Supplementary Information

1. Elemental analysis of the doped ZnO materials by ICP-AES

Inductively coupled plasma atomic emission spectroscopy (Perkin Elmer Optima 7300 ICP-AES) was used to determine the actual contents of Fe and/or Ni dopants in the doped ZnO materials, as summarized in Table S1.

Table S1 Nominal and actual atomic percentages of Fe and Ni atoms in the doped ZnO materials obtained from ICP-AES analysis.

Sample	**Fe loading**		**Ni loading**	
	Nominal (at.%)	Actual (at.%)	Nominal (at.%)	Actual (at.%)
1.0 % Fe-ZnO	1.00	0.69	-	-
0.5 % Fe-ZnO	0.50	0.52	-	-
1.0 % Ni-ZnO	-	-	1.00	1.04
0.5 % Ni-ZnO	-	-	0.50	0.57
0.5 % Ni:Fe-ZnO	0.25	0.18	0.25	0.23
1.0 % Ni:Fe-ZnO	0.50	0.40	0.50	0.54
5.0 % Ni:Fe-ZnO	2.50	2.10	2.50	2.52
10.0 % Ni:Fe-ZnO	5.00	3.94	5.00	4.76

2. High magnification TEM images of the nanorod crystals

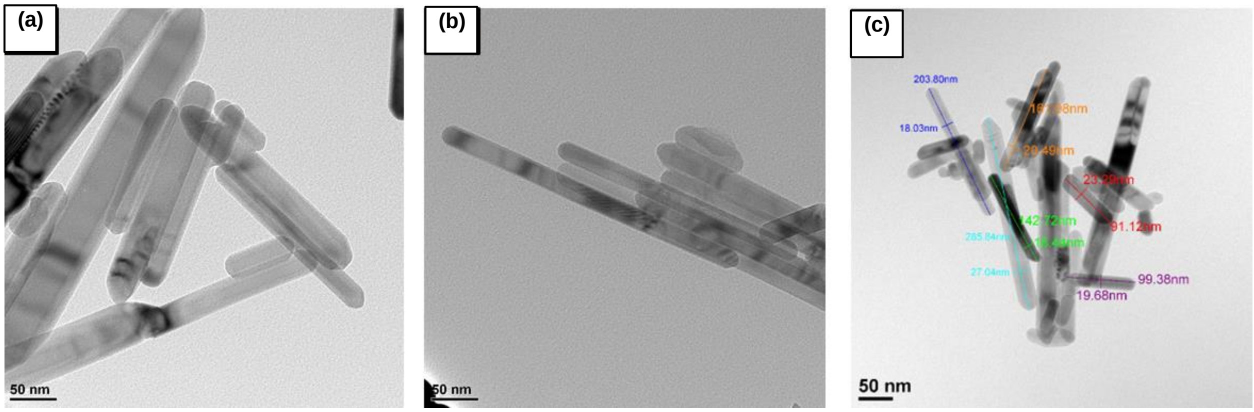

Figure S1 TEM images of the pure ZnO (a), 0.5 % Ni-ZnO (b) and 1.0 % Ni:Fe-ZnO (c) presenting the nanorod structure.

3. High magnification TEM and SEM image of the 6.2% Fe-ZnO sample

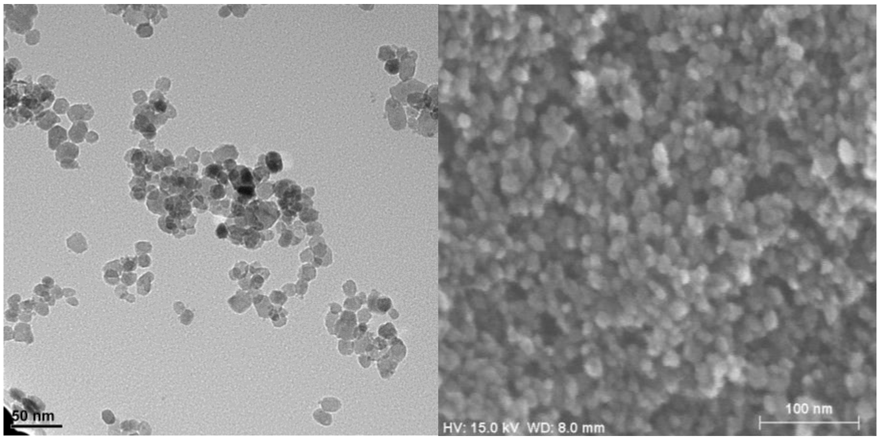

Figure S2 (a) TEM image of the 6.2% Fe-ZnO showing the well-dispersed nanocrystals, and (b) SEM image of the 6.2% Fe-ZnO nanocrystals showing plate-like nanoparticles.

4. Determination of band bap position

In order to calculate the semiconductor band gap, the reflectance data (R) seen in **Figure S3**, was converted into Kubelka-Munk (KM) units by applying the Kubelka-Munk transform, F(R) to the spectra according to Equation (1).

$$F(R) = \frac{(1-R)^2}{2R} \qquad (1)$$

Assuming that the band gap transitions observed in these semiconductor materials follow a direct band gap transition model and that the scattering coefficient is constant in the UV-Vis region the following relation is valid [1]:

$$F(R) \times h\nu = A\left(h\nu - E_g\right)^{\frac{1}{2}} \qquad (2)$$

Where,

$F(R) =$ The sample absorbance in KM units
$h\nu =$ The energy of the incident photon
$A =$ A constant
$E_g =$ The band gap energy of the material

Rearranging the equation for E_g gives,

$$E_g = [\frac{1}{A} F(R) h\nu]^2 + h\nu$$

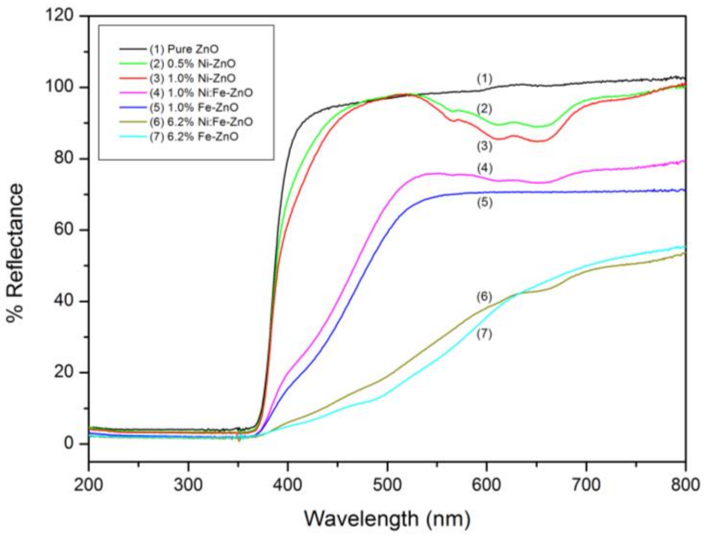

Figure S3 UV-Vis % reflectance data for pure and doped ZnO nanocrystals as used for the Kubelka-Munk transform.

Consequently the band gap energy E_g can be estimated as the straight line intercept of the absorption edge the x-axis of a plot of $[F(R)h\nu]^2$ against $h\nu$ [2]. This is illustrated in **Figure S4** for the pure zinc oxide nanorods.

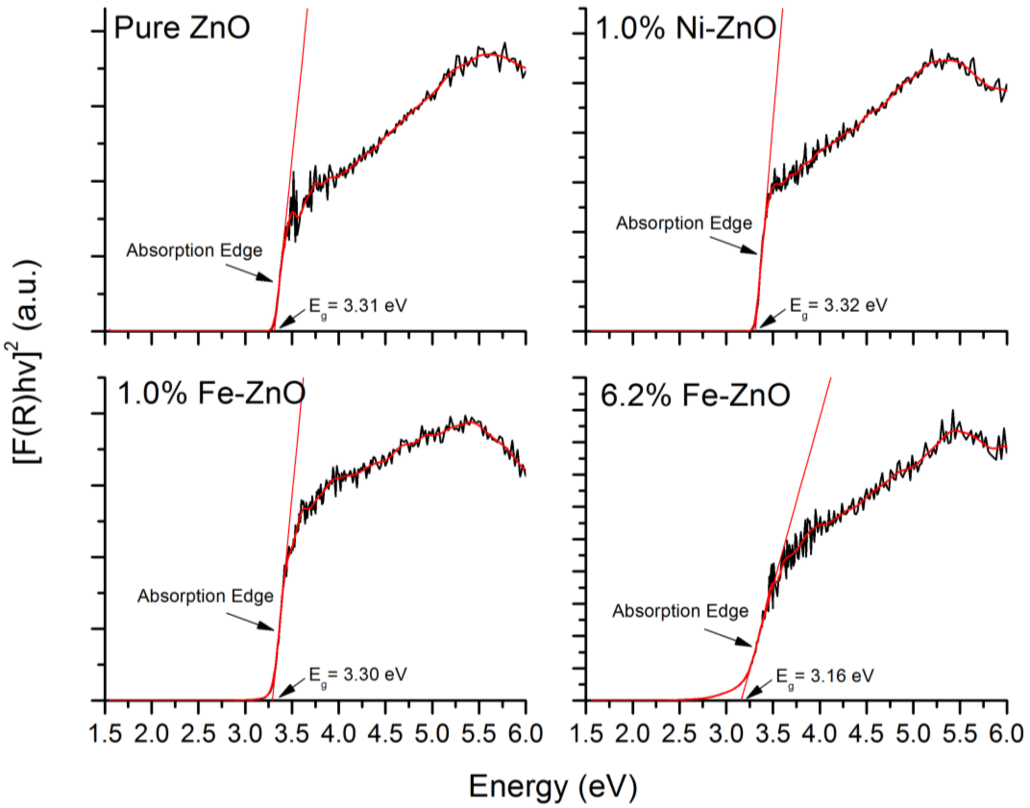

Figure S4 Modified Kubelka-Munk plots, $[\boldsymbol{F}(\boldsymbol{R})\boldsymbol{h\nu}]^2$, showing the absorption edge and band gap positions for a selection of the pure and doped samples. The intercept of the absorption edge represents the band gap position of the semiconductor.

5. Assignment of Raman peaks

As summarized in **Table S2**, all the ZnO-based nanostructures are in the wurtzite hexagonal crystal structure. As such they are members of the C46v (P63mc) space group. Optical phonons arise from the out of phase oscillations of atoms of different mass within a crystal lattice. At the center of the Brillouin zone (Γ point) the phonons will have a non-zero frequency and will create an oscillating dipole moment. As such, the first order Raman scattering will be observed from phonons originating at this point. For these phonons the following optical lattice vibrational modes are predicted by group theory: Γopt = A1(z) + 2B1+E1(x,y)+2E2.

From these, both the A1 and E1 modes induce dipole moments and are thus Raman and Infra-red active and can be further split into two optical components: the transverse optical (TO) and longitudinal optical (LO) modes. The E2 mode is non-polar and consists of high and low frequency phonons arising from sub-lattice (O-O and Zn-Zn) vibrations of the relatively light oxygen atoms (E2high) and lower frequency vibrations of the heavier Zn atoms (E2low). Being non-polar the E2 modes are only Raman active and are silent for infra-red. The two B1 modes (high and low) and silent for both Raman and infra-red and as such will not be addressed. Note that the second order scattering is not limited by these constraints and can combine the effects of different modes originating from different Brillouin points.

Table S2 Room temperature 514 nm Raman peak positions and assignments for the first and second order interactions in pure and doped ZnO nanorods. All peak assignments were derived from the literature [1] with the exception of the $\boldsymbol{E_2^{high} + E_2^{low}}$ mode from the literature [3].

			Peak Position cm^{-1}			
Active mode	**Scattering order**		**ZnO Pure**	**ZnO Ni 0.5 %**	**ZnO NiFe 1.0 %**	**ZnO Fe 0.5 %**
E2 Low	Second		204	204	202	200
E2High-E2Low	Second		331	331	329	327
A1 TO mode	First		380	380	381	-
E2 High	First		437	437	435	434
$\boldsymbol{E_2^{high} + E_2^{low}}$	Second		-	-	522	518
A1LO	First		542	540	544	543
TA+TO	Second		579	577	574	575
TA+LO	Second		620	627	618	616
TA+LO	Second		662	662	656	648

6. EPR spectrum of the pure ZnO nanorods

Generally, pure ZnO is expected to be diamagnetic. Surprisingly, the as-prepared pure ZnO nanorods showed a standard first derivative line shape equating to a g value of 2.2 and a width of approximately 900G (**Figure S5**). Additionally there were a series of paramagnetic signals superimposed onto the broad signal described above which indicate possible defect sites in the crystal. The high-field signal at g = 1.96 may result from shallow donor centres such as ionized impurity atoms within the crystal lattice of ZnO [4]. For instance, carbon atoms possibly remaining from synthesis steps, though usually not paramagnetic, can be ionised to other paramagnetic oxidation states. The low-field signal with a g factor close to the free-electron value (g = 2.01) is attributed to the unpaired electron on oxygen vacancy sites. Jing et al has also reported that the presence of this signal indicates oxygen deficiencies at the crystal surface and arises due to electron trapping at these sites [5].

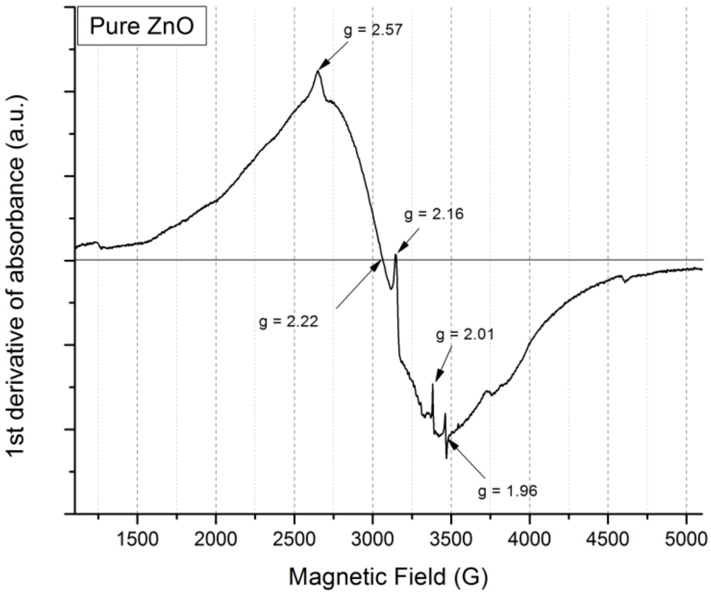

Figure S5 Room temperature EPR spectra of the pure ZnO nanorods

References

1. J. Tauc, R. Grigorovici and A. Vancu, Physica Status Solidi (b), 1966, 15, 627-637.
2. F. C. Jentoft, Electronic spectroscopy: Ultra violet-visible and near ir spectroscopies. In Characterization of Solid Materials and Heterogeneous Catalysts, pages 89-147. Wiley-VCH Verlag GmbH & Co. KGaA, 2012.
3. S. M. Samuel, J. Koshy, A. Chandran and K. C. George, Indian J. Pure Ap. Phys., 2010, 48, 703-708.
4. V. Ischenko, S. Polarz, D. Grote, V. Stavarache, K. Fink and M. Driess. Adv. Funct. Mater., 15(12):1945–1954, 2005.
5. L. Jing, Z. Xu, X. Sun, J. Shang and W. Cai. Appl. Surf. Sci., 2001, 180, 308-314.